# Regional inversion shows promise in capturing extreme-event-driven CO<sub>2</sub> flux anomalies but is limited by atmospheric CO<sub>2</sub> observational coverage

B. Byrne<sup>1</sup>, J. Liu<sup>1,2</sup>, K. W. Bowman<sup>1,3</sup>, Y. Yin<sup>2,\*</sup>, J. Yun<sup>1</sup>, G. D. Ferreira<sup>4</sup>, S. M. Ogle<sup>4,5</sup>, L. Baskaran<sup>1</sup>, L. He<sup>6</sup>, X. Li<sup>7</sup>, J. Xiao<sup>8</sup>, K. J. Davis<sup>9</sup>

<sup>1</sup>Jet Propulsion Laboratory, California Institute of Technology, Pasadena, CA, USA <sup>2</sup>Division of Geological and Planetary Sciences, California Institute of Technology, Pasadena, CA, USA <sup>3</sup>Joint Institute for Regional Earth System Science and Engineering, University of California, Los Angeles, USA <sup>4</sup>Natural Resource Ecology Laboratory, Colorado State University, Fort Collins, CO 80523, United States 10 11 of America Department of Ecosystem Science and Sustainability, Colorado State University, Fort Collins, CO 80523, 12 United States of America <sup>6</sup>Department of Global Ecology, Carnegie Institution for Science, Stanford, CA, United States of America <sup>7</sup>Research Institute of Agriculture and Life Sciences, Seoul National University, Seoul, South Korea 13 <sup>8</sup>Earth Systems Research Center, Institute for the Study of Earth, Oceans, and Space, University of New Hampshire, Durham, NH, USA <sup>9</sup>Department of Meteorology and Atmospheric Science, and Earth and Environmental Systems Institute, 18 The Pennsylvania State University, University Park, Pennsylvania \*Now at Department of Environmental Studies, New York University, New York, NY, USA 19 20 ©2023. All rights reserved. California Institute of Technology, government spon-21

# **Key Points:**

sorship acknowledged.

17

22

- Bottom-up and top-down methods capture reduced 2019 US Midwest carbon up-
- Gaps in atmospheric  $CO_2$  observations drive uncertainties in top-down estimates
- Nested inversion better localizes US Midwest  $\Delta$ NEE relative to coarse global model

Corresponding author: Brendan Byrne, brendan.k.byrne@jpl.nasa.gov

Corresponding author: Junjie Liu, junjie.liu@jpl.nasa.gov

#### Abstract

28

29

30

32

33

34

35

36

37

40

41

42

44

45

46

47

48

49

50

51

52

53

55

56

57

58

59

62

63

65

66

69

70

71

72

74

75

Extreme climate events are becoming more frequent, with poorly understood implications for carbon sequestration by terrestrial ecosystems. A better understanding will critically depend on accurate and precise quantification of ecosystems responses to these events. Taking the 2019 US Midwest floods as a case study, we investigate current capabilities for tracking regional flux anomalies with "top-down" inversion analyses that assimilate atmospheric CO<sub>2</sub> observations. For this analysis, we develop a regionally nested version of the NASA Carbon Monitoring System-Flux (CMS-Flux) that allows high resolution atmospheric transport  $(0.5^{\circ} \times 0.625^{\circ})$  over a North America domain. Relative to a 2018 baseline, we find US Midwest growing season net carbon uptake is reduced by 11-57 TgC (3–16%) for 2019 (inversion mean estimates across experiments). These estimates are found to be consistent with independent "bottom-up" estimates of carbon uptake based on vegetation remote sensing. We then investigate current limitations in tracking regional carbon emissions and removals by ecosystems using "top-down" methods. In a set of observing system simulation experiments, we show that the ability to recover regional carbon flux anomalies is still limited by observational coverage gaps for both in situ and satellite observations. Future space-based missions that allow for daily observational coverage across North America would largely mitigate these observational gaps, allowing for improved top-down estimates of ecosystem responses to extreme climate events.

#### Plain Language Summary

Extreme climate events, such as floods or heatwaves, can have major impacts on the carbon cycle. For example, widespread flooding in the US Midwest during 2019 delayed the planting of crops leading to reduced plant growth and carbon uptake relative to 2018. Here, we test how well this reduction in carbon uptake can be inferred from measurements of atmospheric CO<sub>2</sub>. We find that these data can identify reduced net carbon uptake to the US Midwest during the 2019 floods, but that sparse observational coverage limits our ability to quantify the anomaly in net carbon uptake.

## 1 Introduction

Extreme events, including heat and precipitation extremes, are becoming more frequent (Shenoy et al., 2022; Q. Sun et al., 2021; Kirchmeier-Young & Zhang, 2020; Seneviratne et al., 2021). These events have significant implications for carbon sequestration in terrestrial ecosystems, often causing carbon losses in a single year equal to many years of carbon sequestration (Ciais et al., 2005; Byrne et al., 2021). This is concerning because Nature-based Climate Solutions (NbCSs), which aim to enhance the terrestrial carbon sink through improved land management, have been proposed as an important tool to mitigate CO<sub>2</sub> emissions (Fargione et al., 2018). The increasing frequency of extreme events may disrupt this process, creating a carbon-climate feedback where extreme-event-driven carbon emissions reduce the effectiveness of NbCSs (Zscheischler et al., 2018; Barkhordarian et al., 2021). Consequently, there is an urgent need to quantify the impact of extreme events on carbon uptake by ecosystems for policy programs and other climate applications.

"Top-down" methods offer an approach for estimating biosphere-atmosphere  $CO_2$  fluxes based on observations of atmospheric  $CO_2$ . Typically, Bayesian inverse methods are used to estimate optimal surface fluxes based on constraints from prior information and atmospheric  $CO_2$  observations. Although historically data limited, these techniques are increasingly used to quantify regional carbon cycle responses to extreme events, thanks to expansions of in situ  $CO_2$  measurements and the introduction of space-based retrievals of column-averaged dry-air  $CO_2$  mole fractions  $(X_{CO_2})$  from missions like the Orbiting Carbon Observatory 2 (OCO-2) (Feldman et al., 2023; Byrne et al., 2021). Still, current

capabilities for tracking extreme events are not well understood. This study aims to improve our characterization of these capabilities and identify current limitations.

As a case study, we examine the carbon cycle anomalies from the 2019 US Midwest floods relative to 2018. Intense precipitation during the spring of 2019 (>  $2\sigma$  above average) led to widespread flooding across the US Midwest, a region that accounts for 40% of world corn and soybean production (Yin et al., 2020). Inundation delayed crop planting by 2–3 weeks relative to 2018 across the region, with an additional reduction of 6.8 million hectares in the total planted area (see Fig. 1 of Yin et al. (2020)). These factors led to a 16-day shift in the seasonal cycle of photosynthesis relative to 2018, along with a 15% lower peak value (Yin et al., 2020). In turn, crop yields across the US Midwest were reduced by ~14%, and a decrease in net carbon uptake of ~0.1 PgC was inferred relative to the preceding years (Yin et al., 2020; Balashov et al., 2023). The relatively simple (delayed planting) and well documented carbon cycle perturbation during this event makes it an ideal case study for studying our ability to quantify carbon cycle perturbations using top-down and bottom-up methods. We note that, as we use the single year of 2018 as a baseline, the NEE anomalies inferred will be due to carbon cycle anomalies in both years.

To perform our analysis, we introduce a regionally nested version of the CMS-Flux inversion system with high-resolution  $(0.5^{\circ} \times 0.625^{\circ})$  atmospheric transport over North America (see Sec. 2). This version offers advantages over the coarse-resolution  $(4^{\circ} \times 5^{\circ})$  global version of CMS-Flux. It reduces transport errors introduced by the coarsening of reanalysis winds (Stanevich et al., 2020; K. Yu et al., 2018) and better represents assimilated CO<sub>2</sub> observations, resulting in improved localization of extreme-event-driven CO<sub>2</sub> flux anomalies (Sec. 7.2.2).

The first objective of this study is to evaluate how well existing atmospheric observing systems can quantify flood-induced reductions in carbon uptake during 2019 relative to 2018. We conduct four inversions that assimilate (1) in situ CO<sub>2</sub> measurements (IS), (2) OCO-2 land X<sub>CO<sub>2</sub></sub> retrievals (LNLG), (2) both insitu and OCO-2 land data (LNLGIS), or (4) in situ, OCO-2 land and ocean data (LNLGOGIS)(Sec. 4). Climatological prior fluxes are employed in each experiment, allowing us to attribute posterior anomalies in carbon uptake between years solely to the assimilation of atmospheric CO<sub>2</sub> data. We then compare these estimates with an independent ensemble of remote-sensing bottom-up estimates and with crop-yield data to assess their overall consistency (Sec. 7.1).

The second objective of this study is to assess the impact of existing observational coverage gaps and the potential expansion of space-based  $X_{\rm CO_2}$  measurements on our ability to detect extreme-event-driven anomalies in  $\rm CO_2$  fluxes. To evaluate the effect of expanded space-based observations, we devise a hypothetical observing system that provides daily  $X_{\rm CO_2}$  retrievals at 13:00 local time (similar to OCO-2). Subsequently, we conduct observing system simulation experiments (OSSEs) for existing in situ data and OCO-2 data as-well as the hypothetical observing system. For each OSSE, we evaluate the effectiveness in capturing extreme-event-driven  $\rm CO_2$  flux anomalies (Sec. 7.2.1). Our aim is to gain a deeper understanding of how observational coverage impacts our ability to quantify the influence of extreme events on  $\rm CO_2$  fluxes.

# 2 Nested CMS-Flux inversion system

A one-way nested version of CMS-Flux was developed in this study. Like the global model, this system employs four-dimensional variational data assimilation (4D-Var) to optimize scaling factors on prior land and ocean fluxes. In this section, we describe the nested transport model (Sec. 2.1), boundary and initial conditions (Sec. 2.2), assimilation window (Sec. 2.3), and state vector (Sec. 2.4).

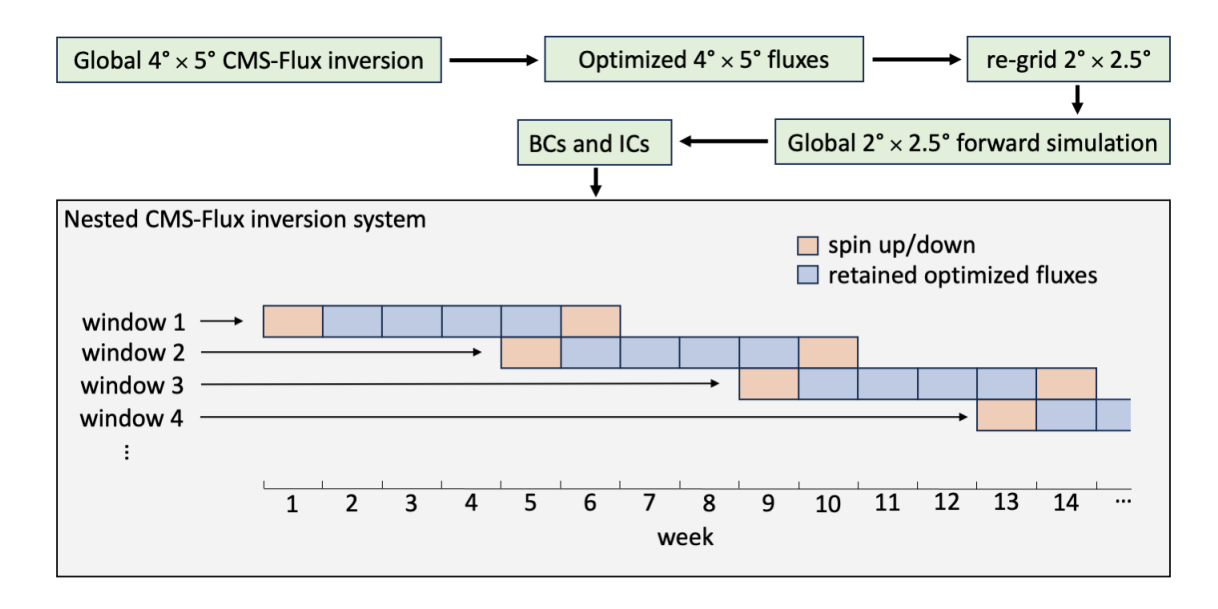


Figure 1. Schematic diagram of the nested CMS-Flux inversion system for North America.

#### 2.1 Nested transport model

We establish a one-way nested inversion system covering the North America region, spanning from  $40^{\circ}$  W to  $167.5^{\circ}$  W and  $14^{\circ}$  N to  $76^{\circ}$  N. Within this domain, model transport is conducted at a spatial resolution of  $0.5^{\circ} \times 0.625^{\circ}$  with a five-minute timestep, using archived MERRA-2 reanalysis data.

# 2.2 Boundary and initial conditions

Boundary conditions (BCs) and initial conditions (ICs) specify the atmospheric  $CO_2$  mole fractions that are imposed on the nested domain. To generate these conditions, we conduct a global  $4^{\circ} \times 5^{\circ}$  4D-Var inversion that optimizes scaling factors on prior land and ocean fluxes. These global inversions utilize the same configuration as Byrne et al. (2020) and match the configuration of the nested inversion. For example, the nested inversion assimilating in situ  $CO_2$  with a CASA-based prior will have boundary conditions from a global inversion assimilating in situ  $CO_2$  with a CASA prior. To generate the boundary conditions, the optimized global net ecosystem exchange (NEE) and ocean fields are regrided and a  $2^{\circ} \times 2.5^{\circ}$  global simulation is run, wherin the BCs and ICs are saved.

#### 2.3 Assimilation window

We use a six-week inversion window and optimize weekly mean land and ocean scaling factors. The middle four weeks of the inversion window are retained as optimized fluxes, while the first and last weeks are excluded as spin-up and spin-down periods. We conduct a batch of eight six-week inversions offset by four weeks, yielding continuous fluxes from April 8th to November 18th. We run these inversions for both 2018 and 2019, resulting in a total of 16 inversion runs. Figure 2 shows a schematic diagram of this setup.

#### 2.4 State vector

CMS-Flux optimizes a vector of scaling factors,  $\mathbf{c} \in \mathbb{R}^M$ . Surface fluxes are obtained by multiplying the scaling factors with an array of control surface fluxes,  $\mathbf{f} \in \mathbb{R}^N$ .

CMS-Flux has the flexibility to optimize scaling factors at coarser spatial and temporal resolution than the native surface flux resolution, such that  $M \neq N$ . In this case, **c** is mapped to the dimension of **f** using a mask,  $\mathbf{A} \in \mathbb{R}^{N \times M}$ :

$$\mathbf{c}_f = \mathbf{A}\mathbf{c}.\tag{1}$$

The surface fluxes,  $\mathbf{F} \in \mathbb{R}^N$  are then obtained by calculating the Hadamard product:

$$\mathbf{F} = \mathbf{c}_f \odot \mathbf{f}. \tag{2}$$

In this study, we optimize scaling factors at coarser spatial and temporal resolution compared to the model. Spatially, a mask is applied to optimize fluxes over a  $4^{\circ} \times 5^{\circ}$  grid, which is truncated at the land-ocean boundary. Temporally, weekly scaling factors are optimized.

#### 2.4.1 Optimized Land fluxes

We aim to optimize weekly-mean net ecosystem exchange (NEE $_{post}$ ) for land areas. However, we do this indirectly by optimizing scaling factors on prior heterotrophic respiration (HR $_{prior}$ ) and subtracting prescribed prior net primary production (NPP $_{prior}$ ):

$$NEE_{post} = c_f \odot HR_{prior} - NPP_{prior}.$$
 (3)

This choice is driven by the improved performance of this configuration during the spring and fall when NEE is close to zero, requiring large scaling factors to adjust the NEE flux. In contrast, HR is always positive and generally significantly larger than zero. The posterior HR fluxes are not interpreted independently but combined with the prior NPP fluxes to obtain a posterior estimate of NEE for analysis.

Prior HR fluxes are calculated by combining prior estimates of NEE and NPP. An ensemble of three prior NEE estimates is obtained from the GOSAT+surface+TCCON experiment of Byrne et al. (2020). These NEE estimates are themselves posterior NEE estimates from inversions that assimilated GOSAT  $X_{\rm CO_2}$ , surface in situ CO<sub>2</sub>, and TC-CON  $X_{\rm CO_2}$  in a global inversion over 2010–2015. The three different NEE estimates differ based on prior fluxes used in the inversions, either CASA, SiB3 or FLUXCOM NEE. We calculate climatological seasonal cycles for each NEE flux over the period of 2010–2015. We refer to the GOSAT+surface+TCCON NEE using a CASA prior as NEE<sub>GIT-CASA</sub>, such that prior HR is calculated as:

$$HR_{prior-CASA} = NEE_{GIT-CASA} + NPP_{prior}$$
 (4)

Prior NPP is estimated from the bottom-up estimates of gross primary production (GPP) (see Sec. 5). First, the 2018–2019 mean seasonal cycle of GPP is calculated across the five estimates, then NEE is taken to be 65% of GPP, NPP<sub>prior</sub> =  $0.65 \cdot \overline{\text{GPP}}$ .

Uncertainties on prior scaling factors are diagonal (only variances) and are based on the spread among the three NEE estimates from Byrne et al. (2020). In addition, uncertainties were inflated when differences between the NEE estimates were small, such as during the spring/fall transition period and in areas with lower productivity (southwestern USA). Finally, these uncertainties were converted into scale factor space by dividing by  $HR_{\rm prior}$ . The prior fluxes, posterior fluxes, and associated uncertainties are provided as supporting information.

#### 2.4.2 Optimized Ocean fluxes

Prior ocean fluxes are similarly derived from the posterior ocean flux estimates of the GOSAT+surface+TCCON experiment by Byrne et al. (2020), and uncertainties on these estimates are diagonal (only variances) and reflect the range among the three experiments that employ different NEE priors.

#### 2.4.3 Unoptimized Fluxes

193

194

195

196

197

198

199

203

204

206

207

210

211

212

213

214

215

218

219

220

221

222

223

226

227

228

229

230

231

232

233

234

235

238

239

240

In addition to the ocean, NPP, and HR fluxes, the forward simulations incorporate prescribed fossil fuel emissions, biomass burning emissions, biofuel emissions, and diurnal NEE. Fossil Fuel emissions used here were specifically made for the v10 OCO-2 modelling intercomparison project (MIP) (Byrne et al., 2023; Basu & Nassar, 2021). Biomass burning emissions are derived from the Global Fire Emissions Database version 4 (GFED4.1s) and scaled to incorporate diurnal variations in emissions (van der Werf et al., 2017). Biofuel emissions are obtained from the CASA-GFED4-FUEL dataset. Diurnal variations in NEE are based on the diurnal NEE variations from the CASA and SiB3 models, as described in Byrne et al. (2020). The SiB3 diurnal cycle is employed for the SiB3-based and FLUXCOM-based NEE priors, while the CASA diurnal cycle is prescribed for the CASA-based inversion. All of these fluxes are regridded from their native spatial resolution to  $0.5^{\circ} \times 0.625^{\circ}$  (fossil fuel emissions were at  $1.0^{\circ} \times 1.0^{\circ}$  degrees, biomass burning emissions were at  $0.25^{\circ} \times 0.25^{\circ}$  degrees, and remaining fluxes were at  $4^{\circ} \times 5^{\circ}$  as archived by Byrne et al. (2020)).

#### 3 Assimilated data

#### 3.1 In situ CO<sub>2</sub>

In situ CO<sub>2</sub> measurements are obtained from version 8.0 of the NOAA GLOBALVIEW plus Obspack dataset (Schuldt et al., 2022). These data are provided on the X2019 CO<sub>2</sub> scale but were back corrected to the X2007 CO<sub>2</sub> scale following Hall et al. (2021). We apply several filters to the in situ data before assimilation. Surface in situ  $CO_2$  measurements are assimilated at their respective height above the surface, with inclusion criteria that the model surface elevation should differ by less than 500 m from the 15 arc-second ETOPO1 global elevation dataset (NOAA, 2021). Secondly, we only assimilate data with the CT\_assim flag greater than or equal to one, which indicates data that is deemed assimilable for the NOAA CarbonTracker system. Finally, only measurements obtained between 11:00 and 17:00 local time are assimilated (when the atmospheric boundary layer is well mixed). The sites assimilated are: amt, bck, bmw, bra, brw, cba, cby, chl, cps, crv, egb, esp, est, etl, fsd, inu, inx, key, kum, lef, lew, llb, sct, sgp, uta, wbi, wgc, wkt, wsa. The sites with CT\_assim≥ 1 that are not assimilated are: mbo, mex, mlo, mwo, nwr, omp, uts, wsd. We note that some sites with CT\_assim= 0 may be assimilable, but more work is needed to characterize their suitability for assimilation. We apply the CT\_MDM "model-data-mismatch" values as uncertainties on assimilated measurements. All aircraft data, including the ACT-America campaign data (Davis et al., 2021, 2018; Wei et al., 2021), are withheld for validation purposes. Monthly maps of data density are shown in Figure S1.

# $3.2 \quad OCO-2 \quad X_{CO_2}$

We employ  $X_{CO_2}$  retrieved using version 10 of NASA's Atmospheric  $CO_2$  Observations from Space (ACOS) full-physics retrieval algorithm (O'Dell et al., 2018). Subsequently, OCO-2 "buddy" super-observations are calculated by averaging individual soundings into super-observations at a spatial resolution of  $0.5^{\circ} \times 0.5^{\circ}$  within the same orbit, assigning equal weights, following the approach by Liu et al. (2017). Monthly maps illustrating data density are shown in Figure S2.

#### 3.3 Ideal LEO pseudo-X<sub>CO2</sub>

We generate pseudo-data for a new hypothetical space-based observing system that provides daily  $X_{\rm CO_2}$  retrievals at 13:00 (1 pm) local time. This hypothetical system, referred to as the ideal LEO mission, could comprise a dense constellation of low Earth orbit (LEO) sensors. The OSSEs are carried out following the same setup as the real data

experiments, while the true atmospheric  $CO_2$  boundary and initial conditions are implemented for the nested inversion.

For the ideal LEO mission, pseudo-observations are generated as follows: 1 pm observations within each land  $0.5^{\circ} \times 0.625^{\circ}$  grid cell are filtered to exclude instances of lowlight conditions, cloudy conditions, and when the surface is covered by snow or ice. Fractional snow cover and cloud cover data are obtained from the MERRA-2 reanalysis dataset (Gelaro et al., 2017). Measurements are excluded for grid cells with a fractional area of land snow cover (FRSNO) greater than 75% and total cloud area fraction (ISCCPCLD-FRC) greater than 75% from the International Satellite Cloud Climatology Project (IS-CCP). Additionally, observations with an atmospheric path exceeding six air-masses are removed. We allow one super-obs within each gridcell per day. The uncertainty on the super-obs is defined to be 0.7 ppm, roughly matching OCO-2. Monthly maps of data density for the ideal LEO mission are shown in Fig. S3.

#### 4 Top-down Experiments

241

242

243

244

245

246

247

250

251

252

253

254

256

257

258

259

260

262

263

264

265

268

269

270

272

273

275

276

277

We perform four different sets of experiments, listed in Table 1. The standard experiment employs the nested model with climatological prior fluxes. The global experiment is conducted to examine the impact of model resolution and follows an identical set-up to the standard experiment but with fluxes regrided to 4°×5°, globally. The IAV experiment is conducted to examine the impact of prior IAV and follows the same setup as the standard experiment but imposes year-specific NPP rather than the 2018–2019 mean (Text. S2).

The OSSEs are conducted to explore the impact of observational coverage in quantifying carbon cycle perturbations resulting from extreme events. These OSSEs cover the same two year period as the real data inversions. True NEE fluxes for the OSSEs are generated by combining a climatological NEE seasonal cycle with anomalies from the bottom-up datasets. Climatological true NEE fluxes are obtained from the CASA-GFED3 model, which undergoes downscaling from monthly to three-hourly fluxes. These fluxes align with those described in Appendix 3 of Byrne et al. (2020). The same unoptimized fluxes are prescribed as described in Sec. 2.4.3. Interannual variations in the true fluxes are introduced by incorporating NEE anomalies taken to be 65% of the mean bottomup GPP anomalies across the five datasets (see Sec. 5). Pseudo-observations are then generated by conducting a forward simulation using the nested model.

**Table 1.** Time of the Transition Between Phase 1 and Phase  $2^a$ 

Experiment	model   Prior	obs	Text section	Figures
Standard	nested clim	real	7.1, 7.2	3, 4, 6, 7, S4, S6, S8, S9, S10, S11, S12
Global	$\mid 4^{\circ} \times 5^{\circ} \mid \text{clim} \mid$	real	7.2.2	7
IAV	nested   year	real	S2	S13, S14, S15
OSSE	nested   clim	pseudo	7.2.1	5, 6

Each experiment described above consists of an ensemble of inversions that assimilate different data sources and employ different priors. A tree diagram illustrating the 12 individual inversions shown for the "standard" experiment are shown in Fig. 2. The diagram shows that four sets of inversions are conducted that differ in assimilated data. The "IS" inversions assimilate in situ CO<sub>2</sub> measurements from the global network of sites

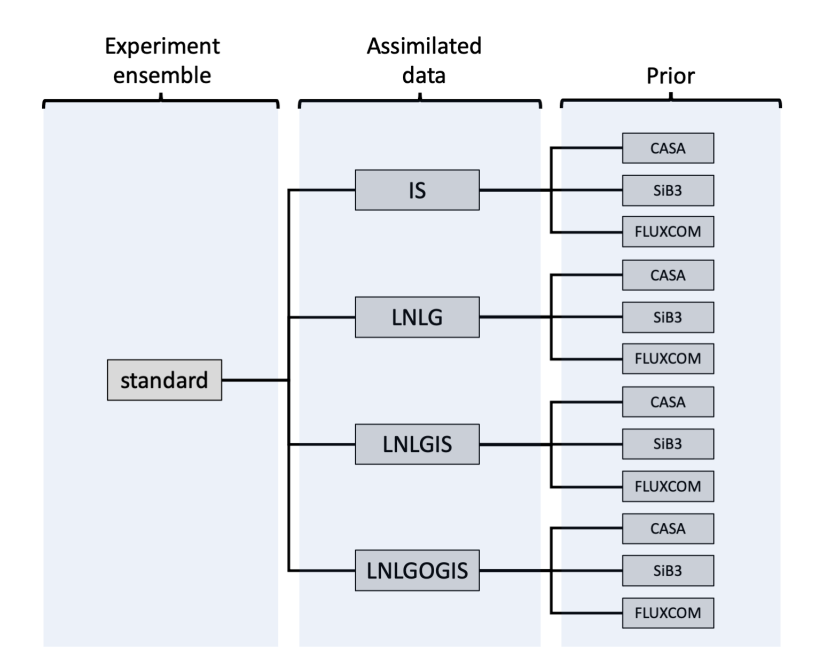


**Figure 2.** Tree diagram showing the 12 inversions conducted for the standard experiment ensemble. For a given experiment, sub-experiments that assimilate different observation using each prior NEE are performed.

(Sec. 3.1). The "LNLG" inversions assimilate OCO-2 land data (Sec. 3.2), including nadir and glint retrievals. The "LNLGIS" inversions assimilate both in situ and OCO-2 land data. Lastly, the "LNLGOGIS" inversions assimilate in situ, OCO-2 land data, and OCO-2 ocean glint retrievals. An additional "ideal LEO" sub-experiment is included for the OSSEs to examine the impact of expanded observations (Sec. 3.3). For each of these datasets, three inversions are performed that differ in prior NEE (Sec. 2.4.1), ocean fluxes (Sec. 2.4.2), BCs and ICs (Sec. 2.2).

# 5 Remote-sensing bottom-up $\Delta$ GPP and $\Delta$ NEE estimates

We generate an ensemble of five bottom-up  $\Delta GPP$  estimates by combining a number of remote-sensing-based GPP datasets. Four of these are obtained from existing datasets: 8 day FLUXCOM remote-sensing-based (RS) GPP (Jung et al., 2020), FluxSat Version 2 (Joiner & Yoshida, 2020), GOSIF GPP (Li & Xiao, 2019), and the NIR<sub>V</sub>-based GPP estimates of L. He et al. (2022). All of these data are regridded from their native resolution to weekly temporal resolution and  $0.5^{\circ} \times 0.625^{\circ}$  spatial resolution.

In addition, we estimate GPP directly from TROPOMI SIF data. This followed the same approach as Yin et al. (2020). Two GPP estimates are then calculated using land-cover-dependent SIF-to-GPP scaling factors from Li et al. (2018) and Y. Sun et al. (2017), which were adjusted by a factor of 0.64 to account for difference retrieval wavelegnths between OCO-2 and TROPOMI (740 nm vs 757 nm). These factors were then applied to gridded SIF data (0.08333° spatial and 8 day temporal resolution), while accounting for the fractional vegetation cover within each griddell. The GPP estimates were then regridded to  $0.5^{\circ} \times 0.625^{\circ}$  spatial resolution. Any data gaps within the growing season are then filled by linear interpolation over time, while GPP is assumed to be zero for data gaps outside the growing season. Finally the two GPP estimates are averaged.

From these GPP datasets, we estimate an anomaly in NEE between 2018 and 2019 by assuming the NEE anomaly is equal to the NPP anomaly, which is itself related to the GPP anomaly by:

$$\Delta NEE = -\Delta NPP = -0.60 \times \Delta GPP \tag{5}$$

The factor of 0.60 is an estimate of the carbon use efficiency (CUE), and is a relatively high estimate (Manzoni et al., 2018; Y. He et al., 2018), though may be representative of corn (S. Yu et al., 2023; Campioli et al., 2015). We assume an error of  $\pm 0.1$  in CUE, and perform error analysis using factors of 0.5 and 0.7. The conversion of  $\Delta$ NPP to  $\Delta$ NEE assumes that  $\Delta$ HR is negligible. This is likely a poor assumption, but a limitation of remotesensing estimates that are insensitive to HR variations. Previously, Yin et al. (2020) showed that bottom-up  $\Delta$ NEE estimated assuming negligible  $\Delta$ HR could reasonably reproduce observed atmospheric CO<sub>2</sub> enhancements during the 2019 US Midwest floods relative to 2018, providing some evidence that  $\Delta$ HR variations have a secondary impact.

# 6 State crop yields and NPP

Crop yields, which represents the amount of crop biomass removed from the field during harvest events, have been estimated using county-level crop yield data from the US Department of Agriculture (USDA) - National Agricultural Statistics Service (NASS) (USDA-NASS, 2020). The carbon content of crop yields was derived from the relationship:

$$Y_{C} = Y_{NASS} \times DM \times C_{f}, \tag{6}$$

where  $Y_C$  is the crop yield, in units of carbon,  $Y_{NASS}$  is the annual county-level crop yield data from USDA-NASS, DM is the dry matter content for each crop, and  $C_f$  is carbon content crop factor. Crop NPP (NPP<sub>crop</sub>), representing the net carbon uptake by crops, was derived from the crop yield estimates using the following equation:

$$NPP_{crop} = Y_{NASS} \times \frac{1}{HI} \times (1 + R_{RS}) \times DM \times C_f,$$
 (7)

where HI is the harvest index for each crop, i.e., the proportion of harvested material (e.g., grains) in relation to total crop aboveground biomass; and RRS is the root:shoot ratio for each crop. We used crop-specific factors for dry matter, root:shoot ratios, harvest indices, and carbon content following the methods in West et al. (2010, 2011) and Ogle et al. (2015). Crop yields and NPP were estimated for over 20 crops, which together represented >99% of total US crop production (USDA-NASS, 2020). Uncertainty in estimates were propagated through a Monte Carlo approach with 10,000 replicates and probability distribution functions for all input data and factors. The results are based on the mean and 95% confidence intervals from the final distribution of simulated values. We note that NASS only included uncertainty in crop yield data for 2020 so we assumed a similar level of uncertainty in crop yields for the other years.

## 7 Results

#### 7.1 2019 minus 2018 NEE anomalies

Figure 3a–b illustrates the difference in June-July NEE between 2019 and 2018 ( $\Delta \text{NEE} = \text{NEE}_{2019} - \text{NEE}_{2018}$ ) for both the remote-sensing bottom-up (ensemble mean) and top-down (LNLGOGIS) estimates. The analyses reveal a significant decrease in CO<sub>2</sub> uptake (positive  $\Delta \text{NEE}$ ) specifically in the US Midwest region. This pronounced positive  $\Delta \text{NEE}$  signal in the US Midwest stands out compared to the rest of the continent. Figure 3c presents the 5 week running mean time series of  $\Delta \text{NEE}$  over the US Midwest. Both the top-down and bottom-up estimates depict a positive  $\Delta \text{NEE}$  signal throughout Jun–Jul, with the anomaly peaking towards the end of June. However, during Aug-Sep, the top-down and bottom-up estimates suggest a negative  $\Delta \text{NEE}$  in the US Midwest. Across the rest of the continent (Figure 3d), anomalies are weaker. The top-down

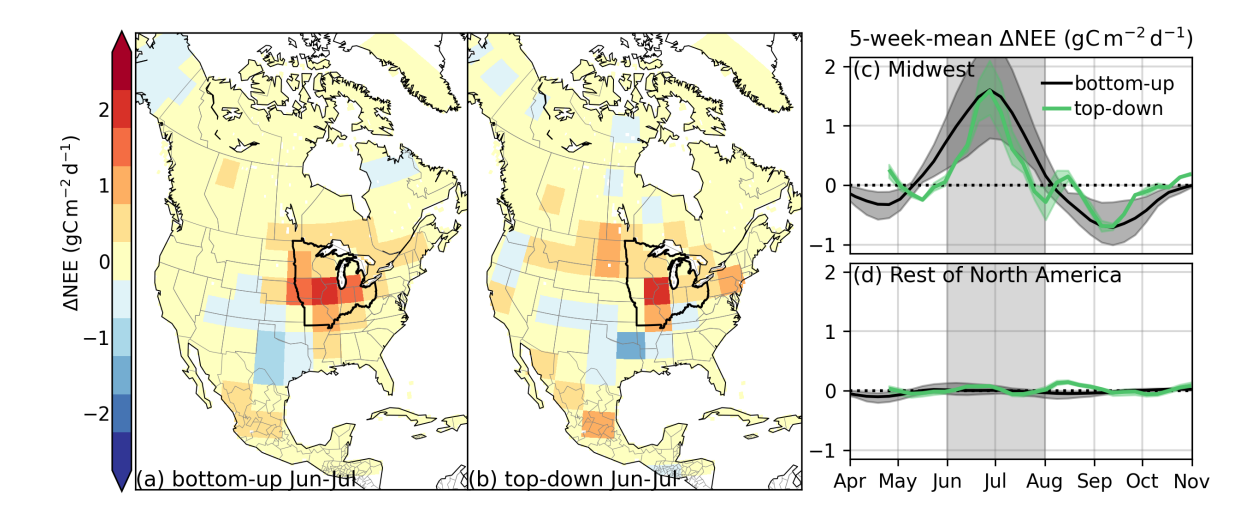


Figure 3. (a) Bottom-up and (b) top-down (LNLGOGIS) spatial patterns of June–July mean  $\Delta \text{NEE}$  (NEE<sub>2019</sub> – NEE<sub>2018</sub>) at 4° × 5° spatial resolution. (c) US Midwest and (d) rest of North America 5-week-mean  $\Delta \text{NEE}$ . The US Midwest is defined as the area within Illinois, Indiana, Iowa, Michigan, Minnesota, Missouri, Ohio, and Wisconsin and is indicated by the black outline in panels (a) and (b). The shading shows the range around the mean estimate for the inversions using three different priors and for the five bottom-up GPP datasets.

estimate suggests a positive anomaly outside the US Midwest during August, while the bottom-up estimate suggests no significant anomalies. The supplementary materials display the maps and timeseries for the other top-down experiments (Fig. S4) and individual bottom-up datasets (Fig. S5).

Figure 4 shows US Midwest  $\Delta$ NEE for each of the top-down and bottom-up estimates. In addition, an estimate of the anomaly in net primary production for crops ( $\Delta$ NPP<sub>crop</sub>) derived from crop yield data is shown. All estimates suggest positive  $\Delta$ NEE over the study period (-6–85 TgC for top-down, 15–78 TgC for bottom-up, and 36–65 TgC for yield-based estimates). We find that June-July  $\Delta$ NEE drives the annual anomaly with uptake reduced by 24–76 TgC in top-down estimates and 38–131 TgC in bottom-up estimates. The bottom-up estimates suggest this is moderated when integrating across the growing season due to greater carbon uptake during Aug-Sep (-56 TgC to -15 TgC), while the top-down estimates are less consistent during Aug-Sep, ranging from -37 TgC to 34 TgC. Figure S6 demonstrates that the bottom-up and top-down  $\Delta$ NEE generally show similar June-July  $\Delta$ NEE across the contiguous United States (CONUS) Climate Assessment Regions. In particular, we find that all estimates obtain negative  $\Delta$ NEE across the Southern Great Plains (-22 to -46 TgC), resulting from the 2018 drought (Turner et al., 2021).

These findings suggest that both in situ and OCO-2 data provide adequate observational coverage to detect the June-July  $\Delta$ NEE signal resulting from the 2019 US Midwest floods relative to 2018. However, some differences are also evident. The experiments disagree in the sign of Aug-Sep  $\Delta$ NEE. The IS experiment shows negative Aug-Sep  $\Delta$ NEE that partially compensates for the positive June–July  $\Delta$ NEE. Conversely, the LNLG experiment gives positive Aug–Sep  $\Delta$ NEE but the smallest June–July  $\Delta$ NEE. There are some spatial differences as-well, for example, the IS experiment suggests larger positive  $\Delta$ NEE in western Canada and negative  $\Delta$ NEE in the southeast during Jun-Jul than the other experiments (Fig. S4). The LNLGIS and LNLGOGIS experiments yield quite similar results. The relative accuracy of these different estimates is challenging to evaluate,

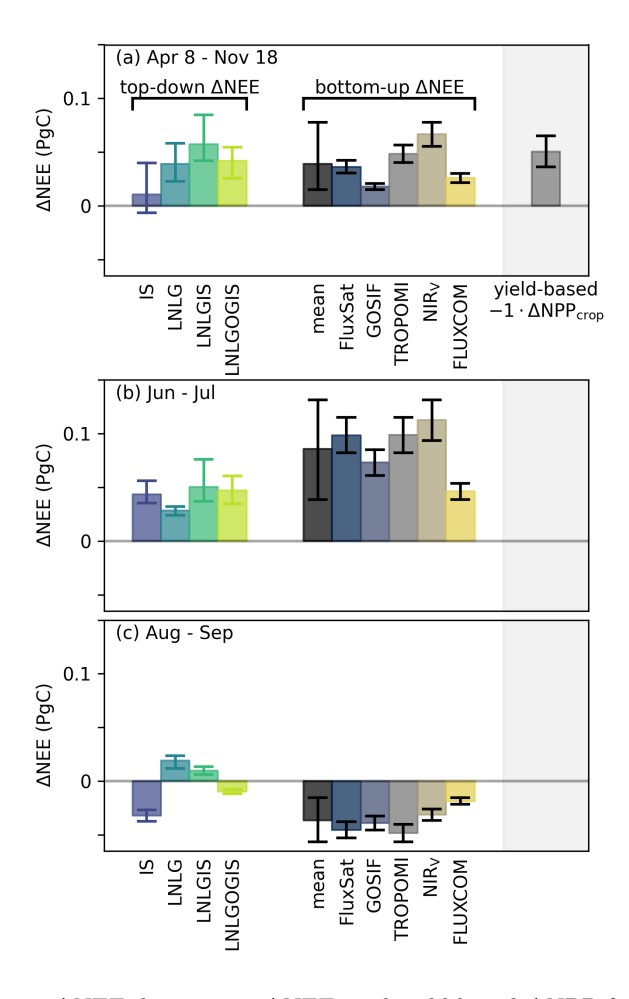


Figure 4. Top-down  $\Delta$ NEE, bottom-up  $\Delta$ NEE, and yield-based  $\Delta$ NPP for crops ( $\Delta$ NPP<sub>crop</sub>) over the US Midwest.  $\Delta$ NEE is calculated for (a) the entire inversion period (April 8th – Nov 18th), (b) June-July and (c) Aug-Sep. The top-down estimates show the mean and range obtained using three different priors. Uncertainty bars for the top-down estimates show the range using three priors, while the uncertainties on the bottom-up show the range of using carbon use efficiencies of 0.5–0.7.

and all experiments exhibit good agreement with independent aircraft CO<sub>2</sub> measurements during 2018 and 2019 (Text S1, Fig. S7-S12). The disparities between experiments may arise from differences in observational coverage and this hypothesis is examined in Sec. 7.2.1.

The bottom-up estimates show some notable differences in the magnitude of  $\Delta$ NEE over the US Midwest and the spatial structure of  $\Delta$ NEE outside the US Midwest (Fig. S5). FLUXCOM consistently displays the weakest  $\Delta$ NEE signal, and has been previously shown to underestimate interannual variations in NEE and GPP (Jung et al., 2020). Outside the US Midwest, the NIR<sub>V</sub>-based estimate shows negative values across the western half of North America, which are not observed in any other estimates, while the TROPOMI-based estimate indicates positive  $\Delta$ NEE across a large portion of eastern Canada. Consequently, the net June–July  $\Delta$ NEE signal outside the US Midwest varies across datasets, ranging from -218 TgC to 187 TgC.

#### 7.2 Sensitivity experiments

# 7.2.1 Impact of observational coverage

Although both the in situ network and OCO-2 were able to identify a positive US Midwest  $\Delta$ NEE signal, we found substantial differences between the top-down experiments. Here, we perform OSSEs to investigate whether gaps in observational coverage could explain these differences. Further, we test whether increased observational coverage (in an ideal LEO constellation) would substantially improve top-down estimates of extreme-event-driven carbon cycle perturbations.

Figure 5 shows the true and posterior  $\Delta$ NEE for the OSSEs. All OSSEs recover positive  $\Delta$ NEE to the US Midwest, consistent with the real data experiments. However, June-July US Midwest  $\Delta$ NEE is underestimated by 43% for IS, 75% for LNLG, 48% for LNLGOGIS and 15% for the ideal LEO constellation. In addition, the inversions tend to introduce a positive June–July  $\Delta$ NEE outside the US Midwest that is not present in the truth. Over June-July, the true continental-scale  $\Delta$ NEE is 89 TgC, while the mean inversion estimates are 163 TgC (error of +74 TgC) for IS, 93 TgC (error of +4 TgC) for LNLG, 68 TgC (error of -21 TgC) for LNLGOGIS, and 93 TgC (error of +4 TgC) for ideal LEO. A similar large continental-scale positive June–July  $\Delta$ NEE was found for the real data IS experiment (Fig. S4ci). One possible explanation is that the limited spatial coverage of the in situ (Fig. S1) data may limit the ability to capture aggregate continental-scale budgets using a one-way nested system.

Overall, the LNLG OSSE shows the worst performance at isolating the US Midwest  $\Delta$ NEE. We suggest that this could be related to interannual variations in the observational coverage. Figure 6a shows that the number of LNLG weekly samplings over the US Midwest can be quite variable from year to year. In particular, there are only 16 super-obs in the US Midwest during the three week period of June 11, 2019 to July 2 2019. This coincides with near zero  $\Delta$ NEE for both the real data LNLG inversion and OSSE (Fig. 6b), and the period with the largest error in  $\Delta$ NEE for the OSSE (Fig. 6c). These results suggest that data gaps in OCO-2, particularly differences in observational coverage between years, limit our ability to estimate inter-annual variations in NEE at high spatio-temporal resolution.

The increased sampling from combining the datasets (LNLGOGIS) appears to moderately improve performance, particularly in isolating June–July  $\Delta$ NEE to the US Midwest (relative to LNLG) and better capturing the continental-scale  $\Delta$ NEE (relative to IS). However, the ideal LEO constellation results in much improved performance in both space and time. The ideal LEO constellation reduces June–July RMSE across  $4^{\circ} \times 5^{\circ}$  regions by 34–51% and the 5-week-mean  $\Delta$ NEE US Midwest RMSE by 55–73%. This comparison suggests that top-down estimates of extreme-event-driven perturbations to

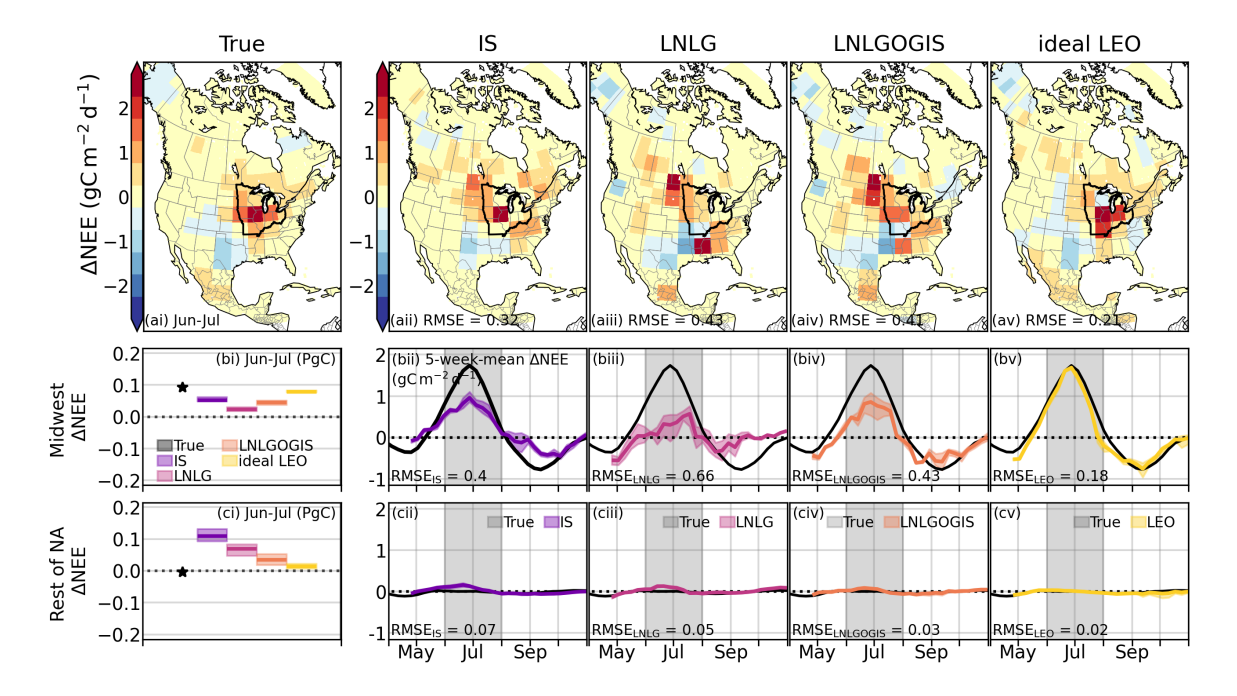


Figure 5.  $\Delta$ NEE estimates for the OSSEs. Panel (ai) shows the true June-July  $\Delta$ NEE maps, while panels (aii)–(av) show the OSSE posterior June-July  $\Delta$ NEE maps and RMSE across grid-cells (gC m<sup>-2</sup> d<sup>-1</sup>). The net US Midwest Jun-Jul  $\Delta$ NEE (PgC) is shown for each OSSE in panel (bi), and the timeseries of 5-week-mean  $\Delta$ NEE is shown for each experiment in panels (bii)–(bv), with RMSE across weeks (gC m<sup>-2</sup> d<sup>-1</sup>). The same quantities are show for the rest of North America in panels (ci)–(cv).

carbon uptake remain observationally-limited and that expanded space-based observing systems will improve these estimates.

#### 7.2.2 Comparison between nested and global inversions

425

426

427

431

432

433

434

435

438

439

440

441

442

443

444

445

The nested CMS-Flux inversion system in this study offers both advantages and disadvantages compared to a global CMS-Flux inversion system. One major advantage is the ability to run transport at a higher resolution  $(0.5^{\circ} \times 0.625^{\circ})$  compared to the global system  $(4^{\circ} \times 5^{\circ})$ . This higher resolution enables tracer transport to be closer to the parent model, as spatial averaging of meteorological fields can average out eddy transport, particularly affecting vertical motions (Stanevich et al., 2020). Additionally, a higher resolution model grid reduces representativeness errors, allowing better representation of fine-scale features that influence observations, such as topography. The primary disadvantage of the one-way nested system used in this study is the assumption of perfect boundary conditions and the inability to assimilate atmospheric CO<sub>2</sub> observations outside the nested domain. In a global inversion, fluxes over North America would impact measurements downwind, providing a powerful constraint on large-scale fluxes, including the net North American flux (Liu et al., 2015). A bias in flux at the continental scale would affect CO<sub>2</sub> fields across the entire Northern Hemisphere. Since the nested inversion lacks this constraint, significant errors in continental-scale fluxes may go undetected. Furthermore, biases in the imposed boundary CO<sub>2</sub> fields can propagate into optimized fluxes.

In order to assess the performance of the one-way nested inversion, we compare the obtained  $\Delta \text{NEE}$  with the global version of CMS-Flux using the same inversion configuration, whenever possible. Figure 7 presents the results for both the global and nested

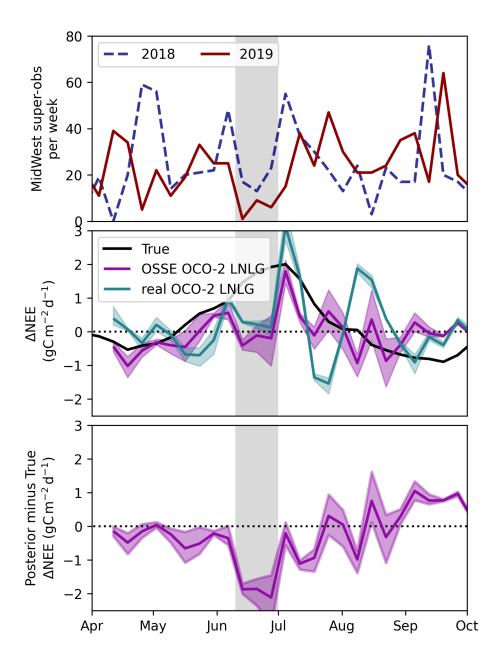
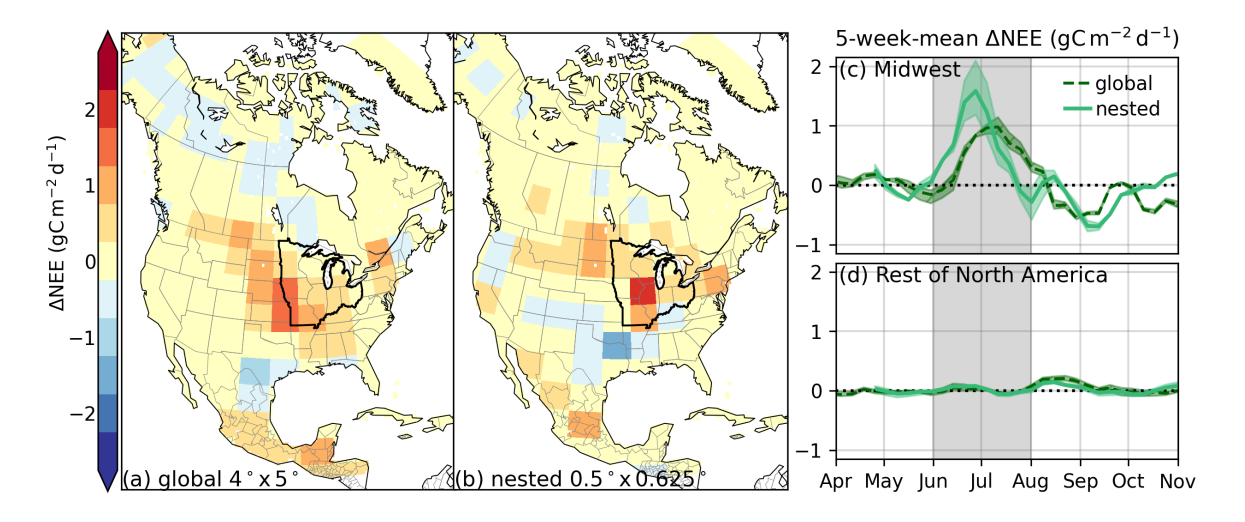


Figure 6. Weekly timeseries of (top) number of OCO-2 super-obs in the US Midwest for 2018 and 2019. (middle) Weekly  $\Delta$ NEE in the US Midwest for the truth, OCO-2 OSSE and real OCO-2 LNLG experiment. (bottom) Difference between posterior and true  $\Delta$ NEE for the OCO-2 OSSE. The shading shows the range around the mean estimate for the inversions using three different priors.



**Figure 7.** Comparison of the global  $4^{\circ} \times 5^{\circ}$  and nested inversion results. Maps of June–July  $\Delta$ NEE from the LNLGOGIS experiment are shown for (a) the global  $4^{\circ} \times 5^{\circ}$  inversion and (b) the nested inversion. Weekly  $\Delta$ NEE in the US Midwest after applying a 5-week running mean are also show for (c) the US Midwest and (d) rest of North America.

versions of CMS-Flux. It is observed that the nested version of CMS-Flux effectively isolates  $\Delta \text{NEE}$  to the US Midwest region during June–July. In contrast, the global model exhibits spatially broader positive  $\Delta \text{NEE}$  across the US Midwest and Great Plains, resulting in a significantly reduced  $\Delta \text{NEE}$  estimate for the US Midwest during June–July. The spatial pattern of  $\Delta \text{NEE}$  for the nested model aligns more closely with the bottomup estimate, suggesting that this system better captures the overall event (although the true  $\Delta \text{NEE}$  is not known). This indicates that, considering the observational coverage provided by LNLGOGIS, the benefits of reduced transport and representativeness errors in the nested model outweigh the detrimental impact of a limited domain.

We note that achieving good performance with nested version of CMS-Flux was challenging, and required a number of trial-and-error inversions. This included varying the size of the state vector spatially  $(0.5^{\circ} \times 0.625^{\circ} \text{ versus } 4^{\circ} \times 5^{\circ} \text{ grid})$  and temporally (weekly, bi-weekly, monthly intervals). It also involved adjusting the prior constraints (optimizing HR rather than NEE, adjusting prior uncertainties). We suggest that these challenges are due to greater regularization requirements for the nested model in comparison to the global model. The sensitivities of observations to surface fluxes are limited to 1–2 weeks by the one-way nesting, such that large-scale constraints are imposed by the boundary conditions (Feng, Lauvaux, Davis, et al., 2019; Feng, Lauvaux, Keller, et al., 2019). Thus, the flux signal in the domain is generally much smaller than for the global model, where downwind observations provide important information for upwind continental-scale regions (Liu et al., 2015). We suggest that imposing an error correlation length between state-vector elements may be an effective approach for regularization in a nested inversion context (see Sec. 8.1), however, this is beyond the scope of our current study.

## 8 Discussion and Conclusions

Both top-down and bottom-up approaches capture a flood-induced reduction in net carbon uptake during the 2019 US Midwest floods relative to 2018. The top-down approach gave mean estimates of 11 TgC (IS), 39 TgC (LNLG), 57 TgC (LNLGIS), 42 TgC (LNLGOGIS) for US Midwest growing season  $\Delta$ NEE. Meanwhile, the bottom-up datasets gave a mean estimate of 39 TgC (range: 15–78 TgC). These magnitudes are significant compared to anthropogenic emissions, amounting to as much as 28% of the US Midwest's annual fossil fuel emissions (300 TgC yr<sup>-1</sup> for 2019, U.S. Energy Information Administration (2023)). In addition, this anomaly is comparable to the year-to-year variations in fossil fuel emissions (SD: 25 TgC yr<sup>-1</sup>), even including the reduction of regional emissions by 36 TgC yr<sup>-1</sup> due to COVID-19 lockdowns in 2020.

In the context of more frequent heat and precipitation extremes (Seneviratne et al., 2021), accurate estimates of the carbon cycle responses will be critical for monitoring carbon budgets and evaluating carbon-climate feedbacks. The results of this study show that both top-down and bottom-up approaches demonstrate skill in capturing  $\Delta$ NEE relative to 2018 resulting from the 2019 Midwest floods, however a number of deficiencies were also identified. In the following sub-sections, we highlight current challenges and opportunities in quantifying carbon cycle extremes.

# 8.1 Top-down

Observational gaps in atmospheric  $CO_2$  observations are identified as a key limitation in applying top-down methods to quantify extreme-event-driven  $\Delta$ NEE, consistent with recent studies of the European carbon budget (W. He et al., 2023; Munassar et al., 2022; Monteil et al., 2020; Thompson et al., 2020). Through a series of OSSE experiments, it was demonstrated that gaps in both the in situ network and OCO-2 sampling impact the accuracy of  $\Delta$ NEE estimates. While assimilating these two datasets concurrently partially mitigates the issue, fully resolving the problem requires expanded ob-

servations. Coverage similar to the ideal LEO observing system could be developed by combining multiple individual satellites, and motivates future studies that assimilate  $X_{CO_2}$  retrievals from multiple space-based observing systems concurrently (e.g., GOSAT, OCO-2, and OCO-3). In addition, efforts should be made to ensure consistency in  $X_{CO_2}$  retrievals between existing and planned missions (e.g., CO2M, GOSAT-GW). Expanding the in situ network would also likely enhance the ability to capture regional flux anomalies more effectively, however, this was not specifically explored.

Although current observing gaps are found to be a major limitation, there may be approaches to better regularize the inverse problem and reduce the impact of these gaps. In particular, applying off-diagonal co-variances in the prior error covariance matrix could be employed to adjust fluxes where observations are missing (Chen et al., 2023). Applying spatial co-variances will likely be especially important for in situ inversions, while applying temporal co-variances may be most useful for OCO-2 X<sub>CO2</sub> inversions. Of course, such an approach will only improve flux estimates if spatial and temporal co-variances are truly present, such that this approach will be limited by a correlation length scale. In addition, imposing realistic prior IAV could also be a fruitful approach, as has been done in previous studies evaluating the 2019 US Midwest floods (Yin et al., 2020; Balashov et al., 2023). However, high-confidence is needed in imposed prior IAV, as inaccurate prior IAV can significantly degrade posterior IAV estimates (Byrne et al., 2019). Text S2 and Figs. S13-15 show that imposing bottom-up IAV in the prior results in larger posterior  $\Delta$ NEE anomalies during the Midwest Floods for all experiments. This is consistent with the  $\Delta$ NEE anomalies being underestimated when using climatological priors, as was found in the OSSEs.

Finally, this study investigated the utility of a one-way nested version of CMS-Flux with  $0.5^{\circ} \times 0.625^{\circ}$  spatial resolution relative to the global model at  $4^{\circ} \times 5^{\circ}$  degree spatial resolution. We note that developing a nested inversion system involved considerable effort in tuning the state vector structure, assimilation window, and prior constraints. Nevertheless, we found that the nested model better allocated flood-induced  $\Delta$ NEE to the US Midwest, suggesting that the improved model transport and observation representation of the nested model improved the overall performance relative to the global model, consistent with several recent studies (Monteil et al., 2020; Hu et al., 2019). However, the nested model has some disadvantages, especially the inability to assimilate downwind observations outside the model domain that may limit the utility of the nested model in other applications. Transport uncertainty and boundary condition errors may lead to significant challenges for nested inversions (Munassar et al., 2023; Kim et al., 2021; Chen et al., 2019; Lauvaux et al., 2012), but were not obvious in our analyses. We note that high-resolution models will be needed to take advantage of upcoming wide-swath sampling missions, such as CO2M ( $\sim$ 250 km swath) or GOSAT-GW ( $\sim$ 400 km swath).

# 8.2 Bottom-up

Remote-sensing-based bottom-up estimates of  $\Delta$ NEE provided a consistent picture of reduced net uptake during the 2019 Midwest floods relative to 2018 but differed significantly in magnitude. The primary source of this variability stems from translating space-based reflectance or SIF observations to GPP, leading to a range in  $\Delta$ GPP between datasets of 120% of the mean. Indeed, estimating the magnitude of GPP from remote sensing datasets is challenging due to satellite signals that could be influenced by factors such as cloud coverage and soil background, in addition to calibration that is predominantly relying on benchmarks provided by eddy covariance sites. We encourage research into approaches that can reduce uncertainties on large-scale GPP magnitudes, possibly through top-down constraints from Carbonyl Sulphide.

Additional uncertainties were introduced in estimating  $\Delta$ NEE from  $\Delta$ GPP. Due to the inherent limitations of remote sensing, which can track GPP but not the total ecosys-

tem respiration (the sum of heterotrophic and autotrophic respiration), certain assumptions must be made. First, to estimate autotrophic respiration, we assumed that  $\Delta$ GPP and  $\Delta$ NPP can be related through a constant carbon use efficiency (CUE) of 0.60 with an uncertainty of range 20% (0.5–0.7), which encompasses most literature estimates. However, in reality the CUR parameter varies across vegetation type, age, and management practices (Campioli et al., 2015; DeLucia et al., 2007; Manzoni et al., 2018; Y. He et al., 2018; S. Yu et al., 2023). Second, we assumed that the influence of  $\Delta$ HR on the  $\Delta$ NEE was negligible. The secondary impact of  $\Delta$ HR is supported by Yin et al. (2020), who were able to reasonably reproduce observed atmospheric CO<sub>2</sub> enhancements during the 2019 US Midwest floods while neglecting  $\Delta$ HR variations. Still, it is important to note that HR is sensitive to variations in temperature and moisture. Terrestrial biosphere models could serve as potential tools for estimating  $\Delta$ HR (e.g., Balashov et al. (2023)) as remote sensing does not adequately capture variations in HR, which is significantly influenced by the availability of labile carbon. However, the accuracy of these model-driven estimates remains challenging to verify.

# 9 Open Research

547

548

551

552

553

555

556

559

560

561

562

579

582

583

585

586

Once accepted for publication, the prior and posterior fluxes, TROPOMI-based GPP, and NIR<sub>V</sub>-based GPP will be archived with a DOI. During the review processes the data 564 are available by contacting Brendan Byrne. The atmospheric CO<sub>2</sub> inversion analyses per-565 formed in this study used the CMS-Flux model, which is based on the GEOS-Chem Ad-566 joint model that can be accessed from the GEOS-Chem Wiki (https://wiki.seas.harvard.edu/geoschem). OCO-2 X<sub>CO</sub>, Lite files can be downloaded from the GES DISC (https://disc.gsfc.nasa.gov). 568 In Situ CO<sub>2</sub> measurements (Schuldt et al., 2022) can be downloaded from https://gml.noaa.gov/ccgg/obspack/. 569 GFED biomass burning emissions (van der Werf et al., 2017) were downloaded from https://globalfiredata.org/. Fossil fuel emissions (Basu & Nassar, 2021) were downloaded from https://doi.org/10.5281/zenodo.4776925. MERRA-2 reanalysis data (Gelaro et al., 2017) was downloaded from https://disc.gsfc.nasa.gov/. 572 TROPOMI SIF data are accessed online at https://data.caltech.edu/records/1347 (DOI: 573 10.22002/D1.1347). FluxSat Version 2 (Joiner & Yoshida, 2021) were downloaded from 574 the ORNL DAAC (https://daac.ornl.gov). GOSIF GPP (Li & Xiao, 2019) were down-575 loaded from http://data.globalecology.unh.edu/. FLUXCOM GPP (Jung et al., 2020) 576 was downloaded from the aata portal of the Max Planck Institute for Biogeochemistry 577 (https://www.bgc-jena.mpg.de/geodb/projects/Home.php).

### Acknowledgments

The research carried out at the Jet Propulsion Laboratory, California Institute of Technology, was under a contract with the National Aeronautics and Space Administration.

Funding for the research was from the NASA CMS (grant nos. 80NSSC21K1060, 80NM0018F0583) and OCO science team (grant np. 80NM0018F0583) programs. Resources supporting this work were provided by the NASA High-End Computing (HEC) program through the NASA Advanced Supercomputing (NAS) Division at Ames Research Center.

# References

Balashov, N. V., Ott, L. E., Weir, B., Basu, S., Davis, K. J., Miles, N. L., ... Stauf-587 fer, R. M. (2023). Flood impacts on net ecosystem exchange in the midwestern 588 and southern united states in 2019. Journal of Geophysical Research: Atmo-589 spheres, 128(18), e2022JD037697. doi: 10.1029/2022JD037697 590 Barkhordarian, A., Bowman, K. W., Cressie, N., Jewell, J., & Liu, J. (2021). Emergent constraints on tropical atmospheric aridity—carbon feedbacks and the future of carbon sequestration. Environmental Research Letters, 16(11), 593 114008. 594 Basu, S., & Nassar, R. (2021, January). Fossil Fuel CO<sub>2</sub> Emissions for the

OCO-2 Model Intercomparison Project (MIP). Zenodo. Retrieved from https://doi.org/10.5281/zenodo.4776925 (Previous versions available from (2018): https://g mao.gsfc.nasa.gov/gmaoftp/sourish/ODIAC/2018/distr ib/, (2017): ftp://aftp.cmdl.noaa.gov/data/ccgg/OD IAC/2017/distrib/, (2016): ftp://aftp.cmdl.noaa.go/v/data/ccgg/ODIAC/2016/distrib/, (2015a): ftp://af tp.cmdl.noaa.gov/data/ccgg/ODIAC/2015a/distrib/) doi: 10.5281/zenodo.4776925 

- Byrne, B., Baker, D. F., Basu, S., Bertolacci, M., Bowman, K. W., Carroll, D., ... Zeng, N. (2023). National CO<sub>2</sub> budgets (2015–2020) inferred from atmospheric CO<sub>2</sub> observations in support of the global stocktake. *Earth System Science Data*, 15(2), 963–1004. Retrieved from https://essd.copernicus.org/articles/15/963/2023/ doi: 10.5194/essd-15-963-2023
- Byrne, B., Jones, D. B. A., Strong, K., Polavarapu, S. M., Harper, A. B., Baker, D. F., & Maksyutov, S. (2019). On what scales can gosat flux inversions constrain anomalies in terrestrial ecosystems? *Atmos. Chem. Phys.*, 19(20), 13017–13035. Retrieved from https://www.atmos-chem-phys.net/19/13017/2019/doi: 10.5194/acp-19-13017-2019
- Byrne, B., Liu, J., Lee, M., Baker, I. T., Bowman, K. W., Deutscher, N. M., . . . Wunch, D. (2020). Improved constraints on northern extratropical  ${\rm CO_2}$  fluxes obtained by combining surface-based and space-based atmospheric  ${\rm CO_2}$  measurements. Journal of Geophysical Research: Atmospheres, 125. doi:  $10.1029/2019{\rm J}{\rm D}032029$
- Byrne, B., Liu, J., Lee, M., Yin, Y., Bowman, K. W., Miyazaki, K., ... Paton-Walsh, C. (2021). The carbon cycle of southeast Australia during 2019–2020: Drought, fires, and subsequent recovery. *AGU Advances*, 2(4), e2021AV000469. doi: 10.1029/2021AV000469
- Campioli, M., Vicca, S., Luyssaert, S., Bilcke, J., Ceschia, E., Chapin III, F. S., . . . others (2015). Biomass production efficiency controlled by management in temperate and boreal ecosystems. *Nature geoscience*, 8(11), 843–846.
- Chen, H. W., Zhang, F., Lauvaux, T., Davis, K. J., Feng, S., Butler, M. P., & Alley, R. B. (2019). Characterization of regional-scale co2 transport uncertainties in an ensemble with flow-dependent transport errors. Geophysical Research Letters, 46(7), 4049–4058.
- Chen, H. W., Zhang, F., Lauvaux, T., Scholze, M., Davis, K. J., & Alley, R. B. (2023). Regional co<sub>2</sub> inversion through ensemble-based simultaneous state and parameter estimation: TRACE framework and controlled experiments. *Journal of Advances in Modeling Earth Systems*, 15(3), e2022MS003208.
- Ciais, P., Reichstein, M., Viovy, N., Granier, A., Ogée, J., Allard, V., ... others (2005). Europe-wide reduction in primary productivity caused by the heat and drought in 2003. *Nature*, 437(7058), 529–533. doi: https://doi.org/10.1038/nature03972
- Davis, K. J., Browell, E. V., Feng, S., Lauvaux, T., Obland, M. D., Pal, S., . . . others (2021). The atmospheric carbon and transport (act)-america mission. Bulletin of the American Meteorological Society, 102(9), E1714–E1734.
- Davis, K. J., Obland, M., Lin, B., Lauvaux, T., O'Dell, C., Meadows, B., ... Pauly, R. (2018). ACT-America: L3 merged in situ atmospheric trace gases and flask data, eastern usa. ORNL Distributed Active Archive Center. Retrieved from https://daac.ornl.gov/cgi-bin/dsviewer.pl?ds\_id=1593 doi: 10.3334/ORNLDAAC/1593
- DeLucia, E., Drake, J. E., Thomas, R. B., & Gonzalez-Meler, M. (2007). Forest carbon use efficiency: is respiration a constant fraction of gross primary production? *Glob. Change Biol.*, 13(6), 1157–1167.
- Fargione, J. E., Bassett, S., Boucher, T., Bridgham, S. D., Conant, R. T., Cook-Patton, S. C., . . . others (2018). Natural climate solutions for the United States. *Science Advances*, 4(11), eaat1869.

Feldman, A. F., Zhang, Z., Yoshida, Y., Chatterjee, A., & Poulter, B. (2023).

Using Orbiting Carbon Observatory-2 (OCO-2) column CO<sub>2</sub> retrievals

to rapidly detect and estimate biospheric surface carbon flux anomalies. Atmospheric Chemistry and Physics, 23(2), 1545–1563. Retrieved
from https://acp.copernicus.org/articles/23/1545/2023/ doi:
10.5194/acp-23-1545-2023

- Feng, S., Lauvaux, T., Davis, K. J., Keller, K., Zhou, Y., Williams, C., . . . Baker, I. (2019). Seasonal characteristics of model uncertainties from biogenic fluxes, transport, and large-scale boundary inflow in atmospheric co<sub>2</sub> simulations over north america. J. Geophys. Res.-Atmos., 124 (24), 14325–14346. doi: 10.1029/2019JD031165
  - Feng, S., Lauvaux, T., Keller, K., Davis, K. J., Rayner, P., Oda, T., & Gurney,
     K. R. (2019). A road map for improving the treatment of uncertainties in high-resolution regional carbon flux inverse estimates. Geophysical Research Letters, 46 (22), 13461–13469. doi: 10.1029/2019JD031165
  - Gelaro, R., McCarty, W., Suárez, M. J., Todling, R., Molod, A., Takacs, L., ... others (2017). The modern-era retrospective analysis for research and applications, version 2 (MERRA-2). *J. Climate*, 30(14), 5419–5454.
  - Hall, B. D., Crotwell, A. M., Kitzis, D. R., Mefford, T., Miller, B. R., Schibig, M. F., & Tans, P. P. (2021). Revision of the World Meteorological Organization Global Atmosphere Watch (WMO/GAW) CO<sub>2</sub> calibration scale. Atmospheric Measurement Techniques, 14 (4), 3015-3032. Retrieved from https://amt.copernicus.org/articles/14/3015/2021/ doi: 10.5194/amt-14-3015-2021
  - He, L., Byrne, B., Yin, Y., Liu, J., & Frankenberg, C. (2022). Remote-sensing derived trends in gross primary production explain increases in the CO<sub>2</sub> seasonal cycle amplitude. *Global Biogeochemical Cycles*, 36(9), e2021GB007220. doi: 10.1029/2021GB007220
  - He, W., Jiang, F., Ju, W., Byrne, B., Xiao, J., Nguyen, N. T., ... others (2023). Do state-of-the-art atmospheric co2 inverse models capture drought impacts on the european land carbon uptake? *Journal of Advances in Modeling Earth Systems*, 15(6), e2022MS003150.
  - He, Y., Piao, S., Li, X., Chen, A., & Qin, D. (2018). Global patterns of vegetation carbon use efficiency and their climate drivers deduced from MODIS satellite data and process-based models. Agricultural and Forest Meteorology, 256-257, 150-158. Retrieved from https://www.sciencedirect.com/science/article/pii/S0168192318300923 doi: https://doi.org/10.1016/j.agrformet.2018.03.009
  - Hu, L., Andrews, A. E., Thoning, K. W., Sweeney, C., Miller, J. B., Michalak,
    A. M., ... van der Velde, I. R. (2019). Enhanced North American carbon uptake associated with El Niño. Science advances, 5(6), eaaw0076. doi: 10.1126/sciadv.aaw0076
  - Joiner, J., & Yoshida, Y. (2020). Satellite-based reflectances capture large fraction of variability in global gross primary production (GPP) at weekly time scales. Agricultural and Forest Meteorology, 291, 108092. Retrieved from https://www.sciencedirect.com/science/article/pii/S0168192320301945 doi: https://doi.org/10.1016/j.agrformet.2020.108092
  - Joiner, J., & Yoshida, Y. (2021). Global modis and fluxnet-derived daily gross primary production, v2. ORNL DAAC, Oak Ridge, Tennessee, USA. doi: 10.3334/ORNLDAAC/1835
- Jung, M., Schwalm, C., Migliavacca, M., Walther, S., Camps-Valls, G., Koirala, S.,

  Reichstein, M. (2020). Scaling carbon fluxes from eddy covariance sites to
  globe: synthesis and evaluation of the FLUXCOM approach. *Biogeosciences*,
  17(5), 1343–1365. Retrieved from https://www.biogeosciences.net/17/
  1343/2020/ doi: 10.5194/bg-17-1343-2020

Kim, J., Polavarapu, S. M., Jones, D. B., Chan, D., & Neish, M. (2021). The resolvable scales of regional-scale co2 transport in the context of imperfect meteorology: The predictability of co2 in a limited-area model. *Journal of Geophysical Research: Atmospheres*, 126 (20), e2021JD034896.

- Kirchmeier-Young, M. C., & Zhang, X. (2020). Human influence has intensified extreme precipitation in North America. *Proceedings of the National Academy of Sciences*, 117(24), 13308-13313. Retrieved from https://www.pnas.org/doi/abs/10.1073/pnas.1921628117 doi: 10.1073/pnas.1921628117
- Lauvaux, T., Schuh, A. E., Uliasz, M., Richardson, S., Miles, N., Andrews, A. E., ... Davis, K. J. (2012). Constraining the co<sub>2</sub> budget of the corn belt: exploring uncertainties from the assumptions in a mesoscale inverse system. Atmospheric Chemistry and Physics, 12(1), 337–354. Retrieved from https://acp.copernicus.org/articles/12/337/2012/ doi: 10.5194/acp-12-337-2012
- Li, X., & Xiao, J. (2019). Mapping photosynthesis solely from solar-induced chlorophyll fluorescence: A global, fine-resolution dataset of gross primary production derived from OCO-2. *Remote Sensing*, 11(21), 2563.
- Li, X., Xiao, J., He, B., Altaf Arain, M., Beringer, J., Desai, A. R., . . . others (2018). Solar-induced chlorophyll fluorescence is strongly correlated with terrestrial photosynthesis for a wide variety of biomes: First global analysis based on OCO-2 and flux tower observations. Global change biology, 24(9), 3990–4008.
- Liu, J., Bowman, K. W., & Henze, D. K. (2015). Source-receptor relationships of column-average  $CO_2$  and implications for the impact of observations on flux inversions. *J. Geophys. Res.-Atmos.*, 120(10), 5214-5236. doi: 10.1002/2014JD022914
- Liu, J., Bowman, K. W., Schimel, D. S., Parazoo, N. C., Jiang, Z., Lee, M., ...

  Eldering, A. (2017). Contrasting carbon cycle responses of the tropical continents to the 2015–2016 El Niño. Science, 358 (6360). Retrieved from http://science.sciencemag.org/content/358/6360/eaam5690 doi: 10.1126/science.aam5690
- Manzoni, S., Čapek, P., Porada, P., Thurner, M., Winterdahl, M., Beer, C., ... Way, D. (2018). Reviews and syntheses: Carbon use efficiency from organisms to ecosystems definitions, theories, and empirical evidence. *Biogeosciences*, 15(19), 5929–5949. Retrieved from https://bg.copernicus.org/articles/15/5929/2018/ doi: 10.5194/bg-15-5929-2018
- Monteil, G., Broquet, G., Scholze, M., Lang, M., Karstens, U., Gerbig, C., ... Walton, E. M. (2020). The regional european atmospheric transport inversion comparison, eurocom: first results on european-wide terrestrial carbon fluxes for the period 2006–2015. Atmospheric Chemistry and Physics, 20(20), 12063–12091. Retrieved from https://acp.copernicus.org/articles/20/12063/2020/ doi: 10.5194/acp-20-12063-2020
- Munassar, S., Monteil, G., Scholze, M., Karstens, U., Rödenbeck, C., Koch, F.-T., ... Gerbig, C. (2023). Why do inverse models disagree? a case study with two european co 2 inversions. *Atmospheric Chemistry and Physics*, 23(4), 2813–2828.
- Munassar, S., Rödenbeck, C., Koch, F.-T., Totsche, K. U., Gałkowski, M., Walther, S., & Gerbig, C. (2022). Net ecosystem exchange (nee) estimates 2006–2019 over europe from a pre-operational ensemble-inversion system. Atmospheric Chemistry and Physics, 22(12), 7875–7892. Retrieved from https://acp.copernicus.org/articles/22/7875/2022/ doi: 10.5194/acp-22-7875-2022
  - NOAA. (2021, July). ETOPO 2022 15 Arc-Second Global Relief Model. NOAA National Centers for Environmental Information. Retrieved from https://doi.org/10.25921/fd45-gt74 doi: 10.25921/fd45-gt74

O'Dell, C. W., Eldering, A., Wennberg, P. O., Crisp, D., Gunson, M. R., Fisher, B., ... Velazco, V. A. (2018). Improved retrievals of carbon dioxide from orbiting carbon observatory-2 with the version 8 acos algorithm. *Atmos. Meas. Tech.*, 11(12), 6539–6576. Retrieved from https://www.atmos-meas-tech.net/11/6539/2018/ doi: 10.5194/amt-11-6539-2018

- Ogle, S. M., Davis, K., Lauvaux, T., Schuh, A., Cooley, D., West, T. O., ... Denning, A. S. (2015, mar). An approach for verifying biogenic greenhouse gas emissions inventories with atmospheric CO<sub>2</sub> concentration data. *Environmental Research Letters*, 10(3), 034012. Retrieved from https://dx.doi.org/10.1088/1748-9326/10/3/034012 doi: 10.1088/1748-9326/10/3/034012
- Schuldt, K. N., Mund, J., Luijkx, I. T., Aalto, T., Abshire, J. B., Aikin, K., . . . van den Bulk, P. (2022). Multi-laboratory compilation of atmospheric carbon dioxide data for the period 1957-2021; obspack\_co2\_1\_globalviewplus\_v8.0\_2022-08-27. NOAA Global Monitoring Laboratory. doi: 10.25925/20220808
- Seneviratne, S., Zhang, X., Adnan, M., Badi, W., Dereczynski, C., Di Luca, A., ... Zhou, B. (2021). [Book Section]. In V. Masson-Delmotte et al. (Eds.), Climate change 2021: The physical science basis. contribution of working group i to the sixth assessment report of the intergovernmental panel on climate change (chap. Weather and Climate Extreme Events in a Changing Climate). Cambridge University Press, Cambridge, United Kingdom and New York, NY, USA: Cambridge University Press. doi: 10.1017/9781009157896.013
- Shenoy, S., Gorinevsky, D., Trenberth, K. E., & Chu, S. (2022). Trends of extreme US weather events in the changing climate. Proceedings of the National Academy of Sciences, 119(47), e2207536119. Retrieved from https://www.pnas.org/doi/abs/10.1073/pnas.2207536119 doi: 10.1073/pnas.2207536119
- Stanevich, I., Jones, D. B. A., Strong, K., Parker, R. J., Boesch, H., Wunch, D., ... Deng, F. (2020). Characterizing model errors in chemical transport modeling of methane: impact of model resolution in versions v9-02 of geos-chem and v35j of its adjoint model. *Geosci. Model Dev.*, 13(9), 3839–3862. Retrieved from https://gmd.copernicus.org/articles/13/3839/2020/doi: 10.5194/gmd-13-3839-2020
- Sun, Q., Zhang, X., Zwiers, F., Westra, S., & Alexander, L. V. (2021). A global, continental, and regional analysis of changes in extreme precipitation. Journal of Climate, 34(1), 243 258. Retrieved from https://journals.ametsoc.org/view/journals/clim/34/1/jcliD190892.xml doi: 10.1175/JCLI-D-19-0892.1
- Sun, Y., Frankenberg, C., Wood, J. D., Schimel, D., Jung, M., Guanter, L., ... others (2017). OCO-2 advances photosynthesis observation from space via solar-induced chlorophyll fluorescence. *Science*, 358(6360), eaam5747.
- Thompson, R. L., Broquet, G., Gerbig, C., Koch, T., Lang, M., Monteil, G., ... others (2020). Changes in net ecosystem exchange over europe during the 2018 drought based on atmospheric observations. *Philosophical Transactions of the Royal Society B*, 375 (1810), 20190512.
- Turner, A. J., Köhler, P., Magney, T. S., Frankenberg, C., Fung, I., & Cohen, R. C. (2021). Extreme events driving year-to-year differences in gross primary productivity across the us. *Biogeosciences*, 18(24), 6579-6588. Retrieved from https://bg.copernicus.org/articles/18/6579/2021/doi: 10.5194/bg-18-6579-2021
- U.S. Energy Information Administration. (2023). Energy-related co<sub>2</sub> emission data tables. https://www.eia.gov/environment/emissions/state/. (Accessed 11 Aug 2023)
- USDA-NASS. (2020). Nass quick stats. USDA National Agricultural Statistics Service. Washington DC.
- van der Werf, G. R., Randerson, J. T., Giglio, L., van Leeuwen, T. T., Chen,

Y., Rogers, B. M., ... Kasibhatla, P. S. (2017). Global fire emissions estimates during 1997–2016. Earth Syst. Sci. Data, 9(2), 697–720. Retrieved from https://www.earth-syst-sci-data.net/9/697/2017/ doi: 10.5194/essd-9-697-2017

- Wei, Y., Shrestha, R., Pal, S., Gerken, T., Feng, S., McNelis, J., ... others (2021). Atmospheric Carbon and Transport–America (ACT-America) data sets:

  Description, management, and delivery. Earth and Space Science, 8(7), e2020EA001634. doi: 10.1029/2020EA001634
- West, T. O., Bandaru, V., Brandt, C. C., Schuh, A. E., & Ogle, S. M. (2011). Regional uptake and release of crop carbon in the united states. *Biogeosciences*, 8(8), 2037–2046. Retrieved from https://bg.copernicus.org/articles/8/2037/2011/doi: 10.5194/bg-8-2037-2011
- West, T. O., Brandt, C. C., Baskaran, L. M., Hellwinckel, C. M., Mueller, R., Bernacchi, C. J., ... others (2010). Cropland carbon fluxes in the united states: Increasing geospatial resolution of inventory-based carbon accounting. *Ecological Applications*, 20(4), 1074–1086.
- Yin, Y., Byrne, B., Liu, J., Wennberg, P. O., Davis, K. J., Magney, T., ... others (2020). Cropland carbon uptake delayed and reduced by 2019 midwest floods. AGU Advances, 1(1), e2019AV000140.
- Yu, K., Keller, C. A., Jacob, D. J., Molod, A. M., Eastham, S. D., & Long, M. S. (2018). Errors and improvements in the use of archived meteorological data for chemical transport modeling: an analysis using GEOS-Chem v11-01 driven by GEOS-5 meteorology. Geosci. Model Dev., 11(1), 305-319. Retrieved from https://www.geosci-model-dev.net/11/305/2018/ doi: 10.5194/gmd-11-305-2018
- Yu, S., Falco, N., Patel, N., Wu, Y., & Wainwright, H. (2023, jun). Diverging climate response of corn yield and carbon use efficiency across the U.S. *Environmental Research Letters*, 18(6), 064049. Retrieved from https://dx.doi.org/10.1088/1748-9326/acd5e4 doi: 10.1088/1748-9326/acd5e4
- Zscheischler, J., Westra, S., Hurk, B. J. J. M. v. d., Seneviratne, S. I., Ward, P. J.,
  Pitman, A., . . . Zhang, X. (2018). Future climate risk from compound events.

  Nature Climate Change, 8(6), 469–477.